Heliyon 10 (2024) e26375

Contents lists available at ScienceDirect

Heliyon

journal homepage: www.cell.com/heliyon

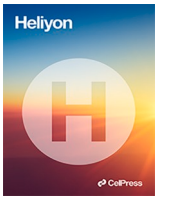

Research article

A biomechanical model of a vehicle passenger in the sagittal plane

Ali Akbari *, Donald Margolis

Department of Mechanical and Aerospace Engineering, UC Davis, CA, USA

ARTICLE INFO

Keywords:
Biomechanical model
Vehicle passenger
Curved motion
Sagittal dynamics
Transmissibility

ABSTRACT

Musculoskeletal biomechanical models have wide applications in ergonomics, rehabilitation, and injury estimation. Their use can be extended to enable quantitatively explaining and estimating ride comfort for a vehicle's passenger. A biomechanical model of the upper body in the sagittal plane is constructed, which allows for curved motion to simulate the propagation of disturbance energy within a seated passenger aboard a moving vehicle. The dynamic predictions of the model are validated against experimental results within the literature. Frequency responses show that within the vehicular frequency range, the L4L5 and the L5S1 discs in the lower lumbar region are susceptible to the highest vibration transmission. It was also found that vibration transmission is maximized at around 4.5 Hz. The model provides analytical and geometric intuition into the motion of the various segments of the upper body using a few simple geometric assumptions and can be employed to develop a quantitative ride-comfort metric, such that the most comfortable ride would be that which would induce the least internal motion within the passenger model.

1. Introduction

With the rise of autonomous vehicles and automotive manufacturers competing for the vehicle market, ride comfort is continuously becoming increasingly important [1]. Several factors affect a passenger's perception of ride comfort, including non-mechanical aspects such as temperature, air quality, or auditory noise [2]. The mechanical factor that impacts ride comfort is known to be vibration [3]. The ride comfort indices that are available in the literature have certain shortcomings. Most are subjective, i.e., the same excitation has been perceived differently amongst different test subjects. For example, Els [4] showed that ride comfort was felt differently amongst various occupations, such that soldiers rarely claimed discomfort, while managers rarely claimed comfort when exposed to the same ride conditions. In another instance, Yang et al. [5] demonstrated that the same peak acceleration had resulted in ride evaluations ranging from "comfortable" to "very unsatisfactory", and Oborne [6] argued that experimental ride comfort tests were inconclusive, as the same vertical acceleration in both frequency and magnitude content was perceived differently ranging from "almost very good" to "more than uncomfortable". Furthermore, the currently available ride comfort metrics have discrepancies in identifying the agent responsible for ride comfort. Amidst the various kinematic input signals, some studies suggest that it is acceleration [7] that mainly impacts ride comfort, while others claim it is jerk [8], and a few others argue that it is a combination of both signals [1]. Additionally, studies mostly claim vertical motion to be of utmost importance [9], whereas other studies argue longitudinal [10] or lateral [11] motion might also be important. There are a few widely established industrial standards for ride comfort, such as ISO2631 [9], BS6841 [12], and VDI2057 [13], that focus on vertical acceleration as the major responsible agent for ride comfort. While they all agree on the trend that increasing acceleration reduces comfort, their zones of comfort do not overlap [4], such that a hypothetical ride that pushes

* Corresponding author.
E-mail addresses: alakbari@ucdavis.edu (A. Akbari), dlmargolis@ucdavis.edu (D. Margolis).

https://doi.org/10.1016/j.heliyon.2024.e26375
Received 2 May 2023; Received in revised form 4 February 2024; Accepted 12 February 2024
Available online 16 February 2024

ISO2631 to its threshold of discomfort is considered "very uncomfortable" according to BS6841 and "comfortable" according to VDI257.

To address the issues above, a quantitative ride comfort metric is required that can estimate the effect of input vibrations on the passenger's body. It is hypothesized that having knowledge of the internal dynamics of a passenger's body enables one to make a ride comfort inference according to its dynamic response. A novel ride comfort metric could be introduced that correlates discomfort with the motion deviation of the elements within the passenger's body. In this analogy, the most comfortable ride would be that which has induced the least amount of displacement deviation within the passenger body's internal biomechanics.

Should such a metric be available, one can quantitatively associate controllable vehicle kinematic signals with ride comfort and develop vehicle control algorithms accordingly or design vehicle systems such as seat or suspension to achieve maximum ride comfort. This provides the motivation for developing a biomechanical model of a vehicle's passenger. However, biomechanical models have quite diverse applications in injury estimation [14], ergonomics [15] and rehabilitation [16]. Therefore, the use of the proposed model would not be restricted to ride comfort assessment.

Most available passenger biomechanical models have investigated the vertical motion within the body, as it has been argued that it is the vertical vibration, also known as the heave motion, that impacts ride comfort the most [9]. Many of them adopt lumped-parameter modeling and comprise a few inertial elements connected vertically contiguously with springs and dampers in between them where the masses possess vertical degrees of freedom. Gohari and Tahmasebi [17] designed an active suspension control strategy that minimized the displacement of the head in a two-degree-of-freedom vertical passenger model. Kuznetsov et al. [18] employed ISO2631's ride comfort metric to optimize a quarter-car suspension system using a one-degree-of-freedom vertical passenger model. Using finite element analysis, Dong et al. [19] showed that seat stiffness and sitting posture affect the passenger body's internal dynamic response. Guruguntla and Lal [20] established a ten-degree-of-freedom vertical biomechanical model of the upper body and found an optimized set of parameters for their particular model. They asserted that their model replicated real human response to vibration better than two, four, or seven-degree-of-freedom models. Cho and Yoon [21] developed a nine-degree-of-freedom passenger model to evaluate ride quality that included longitudinal degrees of freedom as well as vertical. They concluded that including the backrest support in the model is essential because of its effect on the natural frequencies and argued that simpler one, two, or three-degree-of-freedom, vertical-only models did not match experimental vibration transmissibility as well as the sophisticated nine-degree-of-freedom model. Mohajer et al. [22] developed an intricate, 28-degree-of-freedom, three-dimensional, non-linear, integrated seat-human biomechanical model and adopted ISO2631 to associate the RMS acceleration of individual body segments with an estimation of ride comfort. They concluded that ride comfort had the highest correlation with vertical and longitudinal vibrations

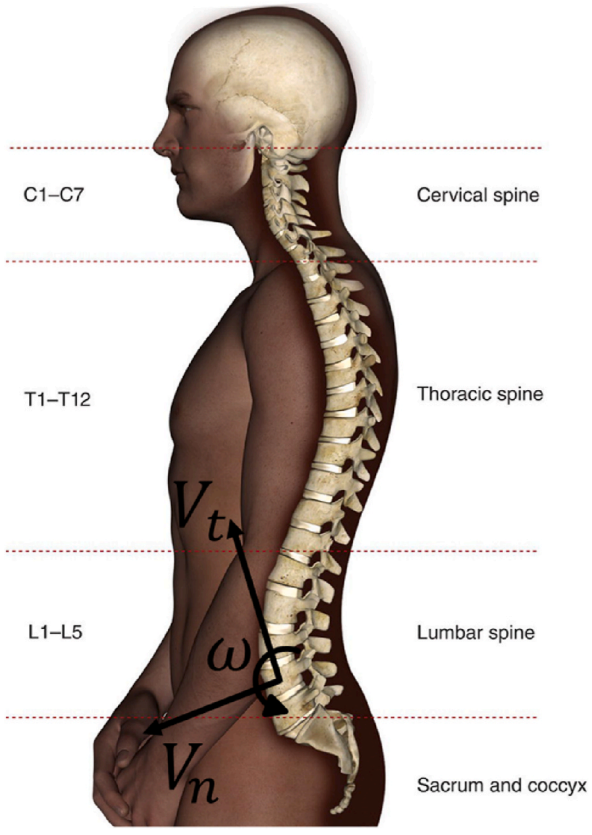

Fig. 1. Sagittal view of the spinal column and its different sections [27].

within the passenger's body. Liang and Chiang [23] developed a 14-degree-of-freedom biomechanical model of a seated human body and stressed that for the responses of a seated body to vertical vibrations to match experimental data, the mathematical modeling must be at least two-dimensional within the sagittal plane, which is defined as the longitudinal plane that divides a bilaterally symmetrical body into right and left sections. Kim et al. [24] determined the necessary number of lumps to consider in a model that would correspond well with experimental tests in terms of vibration transmissibility. Kozawa et al. [25] showed that seated vehicle passengers feel the most discomfort due to the vertical vibrations from the seat's hip cushion and vertical/longitudinal vibrations from the seat's backrest cushion, and not those that come in through the feet.

According to the results of this previous research, the proposed biomechanical model need only include the upper body. The upper body's mechanical structure primarily consists of the human spine stretched between the pelvis and the head. Because of the spine's inherently curved, S-shaped geometry [26], even if it is only the vehicle's vertical vibration input that is to be considered, its mechanical effects within the body still cannot be properly accounted for using a vertical-only model. Consequently, the model of interest needs to encompass the necessary degrees of freedom, but not more, to maintain simplicity and yield physical intuition.

Based on the reviewed literature, to be able to make inferences on ride comfort as a function of internal displacements within the passenger body in response to disturbance vibrations coming from the vehicle, it is necessary to develop a biomechanical model of the passenger's upper body in the sagittal plane that can support curved geometry and motion and also has sufficient degrees of freedom to correspond to experimental vibration transmissibility data.

2. Modeling

According to Ref. [25], the comfort-determining vibrations lie in the vehicle's pitching plane, i.e., the plane within which the vehicle rotates around its lateral axis. Said plane includes the cruise (longitudinal) and heave (vertical) translations as well as the pitch rotation. In the passenger body's anatomical terms, that plane coincides with the sagittal plane. The spinal column itself is made up of three major sections which are distinguished from one another according to changes in the direction of spinal curvature [26]: the lumbar spine (lowermost section), the thoracic spine (middle section), and the cervical spine (uppermost section) as seen in Fig. 1.

The passenger model should account for the most prominent motions in the sagittal plane and the mechanical elements that affect them significantly. It should be noted that even though the model at hand is meant for the purpose of assessing a passenger's internal dynamics while aboard a moving vehicle, its design is sufficiently generic to be used in any application that requires a biomechanical model of the upper body in the sagittal plane.

2.1. Building blocks and structure

Decades-long cohort studies have shown that lower back pain, a medical condition associated with the lumbar spine, is among the most common and costly musculoskeletal disorders [28]. Among the three different spinal sections, the lumbar spine bears the highest portion of the weight of the upper body, has the largest range of motion [26], and is closest to the load input (hip cushion) for a vehicle passenger. It is also evident that the lumbar spine is prone to the highest levels of chronic and acute pain [26]. Thus, the lumbar spine is of utmost importance when constructing a biomechanical model of the upper body. The lumbar spine itself comprises five lumbar vertebrae, named L1 through L5, that sandwich the intervertebral discs which are named according to the vertebrae to which they are attached on either side and provide compliance and damping. The vertebrae are mechanically much harder than the discs [29] and are therefore modeled as rigid body inertias while the discs are modeled as springs and dampers.

The thoracic spine is the middle segmental column of the upper body that is connected to the ribcage and shapes a relatively rigid casing around the internal organs. Morita et al. [30] showed that the thoracic range of motion is significantly smaller than that of the lumbar. Also, the thorax altogether is one relatively large inertia, almost an order of magnitude more massive than the most massive lumbar vertebra [31]. Subsequently, it is reasonable to assume the entire thorax as one rigid body despite entailing 12 of the total 33 vertebrae in the spinal column [26].

The head rests on the neck, which comprises seven cervical vertebrae [26]. Generally, the cervical vertebrae have a significant range of rotary motion with respect to one another. However, a vehicle's passenger would most probably be looking ahead, and the motions induced by a vehicle would not be outside a linear range of motion. Thus, one equivalent neck joint is used to adequately approximate the cervical spine in this model.

At the bottom of the passenger model lies the pelvis, which is modeled as a large inertia that serves as the base for the rest of the passenger model.

Another mechanical element in the upper body that could affect internal sagittal motions is the musculature. There is a plethora of muscle fibers pulling on various vertebrae, but they are clustered into main muscle groups [32]. In the sagittal plane, muscles are either flexors that bend the upper body forward or extensors that bend it backward. Due to the seat's backrest, in the case of a seated passenger, there would generally be no extension motion as a passenger cannot bend backward with the seat's backrest at their back. Therefore, only extensor muscles are of interest. Additionally, the low-amplitude flexion motions of a passenger would generally include no active bending, such as the case of intentional, large-scale forward bending. Hence, muscles would be modeled to act only passively, which can be approximated by an elastic resistance to tension. Consequently, one local multifidus muscle is considered for each lumbar vertebra, and one global longissimus muscle is considered for the thorax. Muscles are attached to the pelvis and passively resist forward bending if in tension.

The only remaining part of the upper body would be the arms. The arms are excluded from the model since the passengers of an autonomous vehicle would most likely have their arms rest on their laps, and therefore the arms wouldn't impact sagittal motions

significantly. However, having the arms resting on a steering wheel would somewhat affect the dynamic response of the model, as shown by Pranesh et al. [33].

Finally, the seat acts as the source of input excitations coming from the vehicle and includes a hip cushion, modeled as a translational point mass plus a spring and a damper, and two backrest cushions for lumbar and thoracic support, which are modeled as springs and dampers. These supports exert forces on the passenger model in a direction perpendicular to the seat.

The planar degrees of freedom within the geometry of the sagittal spine correspond to axial displacement (tangent to the spine along the spinal cord), anterior-posterior shear displacement (perpendicular to the spine and the spinal cord), and flexion/extension

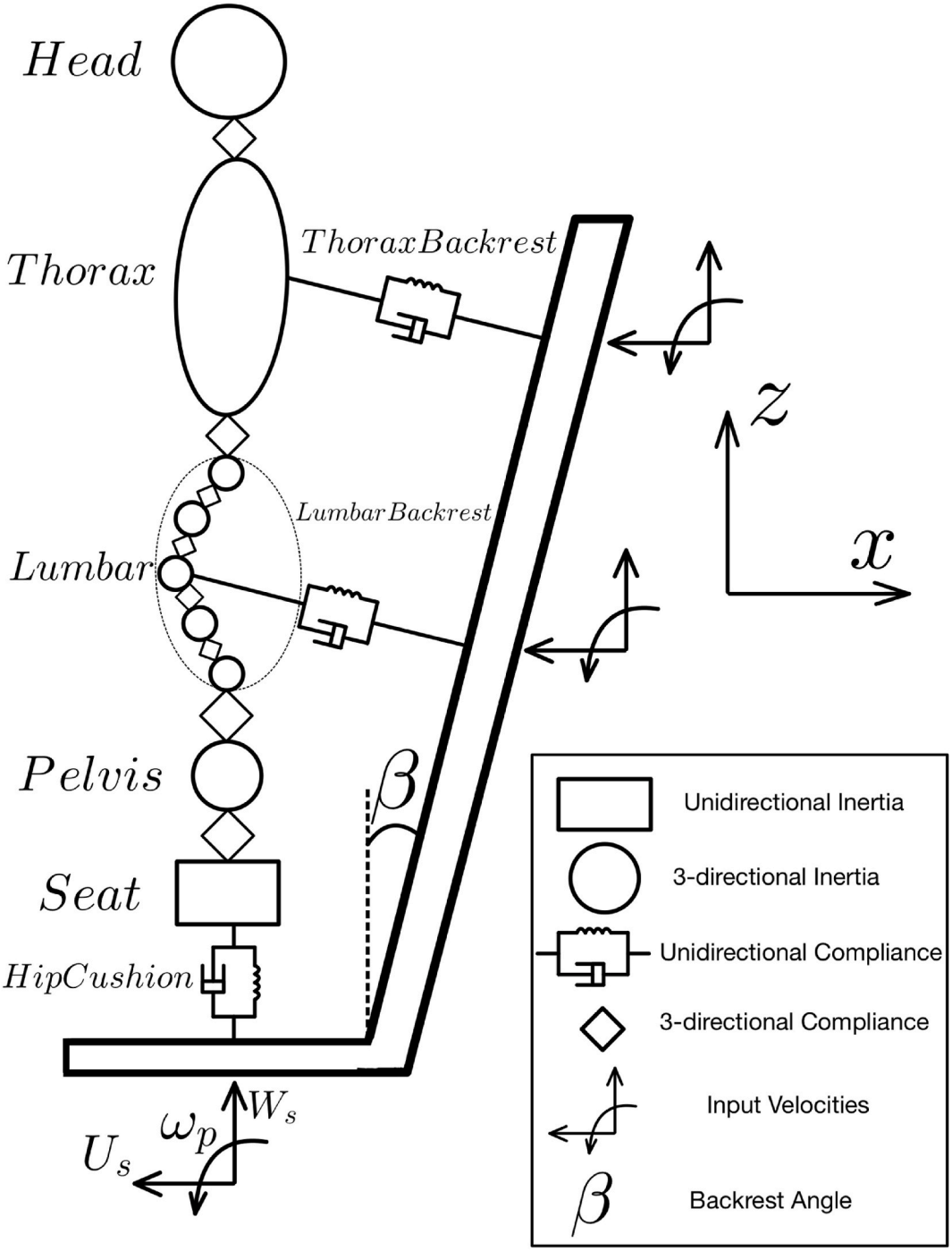

Fig. 2. Schematic of the passenger model.

rotation (bending forward or backward) as shown in Fig. 1. These directions constitute the necessary and sufficient degrees of freedom for constructing a passenger biomechanical model which can appropriately investigate the propagation of a vehicle's major input vibrations within the body. To sum up, the passenger model would include eight inertias, including the pelvis, the L5 through L1 vertebrae, the thorax, and the head. In between all these would be elements that provide stiffness and damping. Each inertia has three sagittal degrees of freedom, and the hip cushion has one degree of freedom perpendicular to the seat. This results in a 25-DOF model. A schematic of the model is shown in Fig. 2.

The rhombus shapes in Fig. 2 represent 3-directional spring/damper elements, which provide stiffness and damping in all three axial, shear, and rotary directions. There is also a distinction between the seat mass, which can only move perpendicular to the hip cushion, and the remaining inertias, which can both translate and rotate in the sagittal plane and have a rotational inertia component as well as mass. Furthermore, the input signals to the passenger model are heave (vertical W_s), cruise (longitudinal U_s), and pitch (rotational ω_p) velocities, which come from a separate vehicle model and are calculated at the point of contact of the seat with the passenger model using velocity transfer from the vehicle's center of gravity. Also, the seat is allowed to have a backrest inclination angle β, which is zero if the seat is upright.

2.2. Physical assumptions

There are quite a few challenges in modeling biomechanical systems. These include but are not limited to parts having freeform, organic geometries, mechanical elements possessing complicated constitutive behaviors, and their characteristic parameters displaying great uncertainty. Thus, making certain modeling assumptions is necessary in developing biomechanical models. The most prominent physical assumption in developing the passenger model at hand is perhaps that force-generating elements, i.e., springs and dampers, have linear constitutive behaviors. This means that spring forces are proportional to the displacement across the spring, and damper forces would be proportional to the relative velocity across the damper. In reality, it is known that such elements do not generally display linear behavior [34] and are prone to non-linear effects such as viscoelasticity [35], poroelasticity [36], and hysteresis [37]. However, studies show that the force-generating elements behave rather linearly in the low-amplitude range of motion for both rotation [38] and translation [39]. Given that this model is generally not intended for large displacements or impact loads, assuming linear constitutive behavior for force-generating elements is reasonable.

2.3. Geometry and kinematics

The model accounts for the curved geometry of the spine. Therefore, body-fixed, curvilinear coordinates are used, and each inertia is assumed to have three sagittal velocity components: a tangential velocity V_t along the spinal cord, a normal velocity V_n perpendicular to it, and an angular velocity ω. Also, to have access to the angular orientation of each inertia, the angle θ is designated as the angle that the tangential velocity component makes with respect to the inertial x direction, as depicted in Fig. 3. The spinal degrees of freedom are also shown in Fig. 1.

The body-fixed velocities can be projected along the inertial directions and integrated so as to obtain inertial displacement and angular positions, as given in Eqs. (1)–(3):

$$\theta(t) = \int \omega \mathrm{d}t + \theta_0 \tag{1}$$

$$x(t) = \int (\, V_t \cos\theta - V_n \sin\theta \,)\mathrm{d}t + x_0 \tag{2}$$

$$z(t) = \int (\, V_t \sin\theta + V_n \cos\theta \,)\mathrm{d}t + z_0 \tag{3}$$

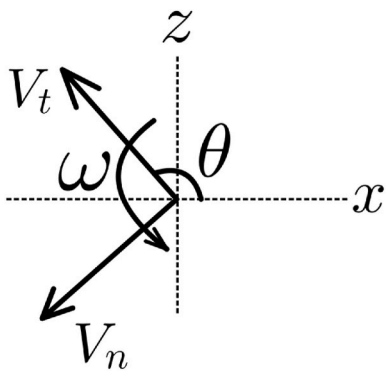

Fig. 3. Schematic of body-fixed velocities for each inertia.

where $x(t)$ and $z(t)$ represent the instantaneous translational position of the center of gravity of the inertial element with respect to the inertial x–z frame, and θ(t) indicates its angular position with respect to the positive x-direction. The coordinate origin is the seat base in the hip cushion.

The instantaneous directions of axial compliance and shear compliance need to be expressed in terms of the instantaneous positions of the inertias. The cornerstone in shaping the geometry of this model is the assumption that the intervertebral axial compliance lies in the direction of the line that connects the centers of gravity for the two adjacent inertias. Once that direction is obtained, the direction of the shear compliance would be perpendicular to that line. In an exaggerated fashion for the purpose of clarity, Fig. 4 shows the centers of gravity for two consecutive top (T) and bottom (B) inertias, along with their individual velocity components and the directions for axial and shear compliance.

Axial and shear forces would respectively be in the direction of $\mathbf{e_a}$ and $\mathbf{e_s}$ which are unit vectors for axial and shear directions and are determined by the angle φ. The φ angle can be obtained in terms of inertial positions according to Fig. 4 as follows in Eq. (4):

$$\varphi = \tan^{-1}\frac{z_T - z_B}{x_T - x_B} \tag{4}$$

It's noteworthy that the two inertias share a φ angle which would thusly be uniquely found, as both $z_T - z_B$ and $x_T - x_B$ are individually available. In turn, the contribution of the intervertebral compliance forces to the body-fixed velocities would be determined by the difference between the φ angle and the inertia's individual θ angles, which are denoted with ψ_T for the top and ψ_B for the bottom inertia. With knowledge of φ, Eq. (5) gives ψ_T and ψ_B:

$$\psi_T = \varphi - \theta_T \quad ; \quad \psi_B = \theta_B - \varphi \tag{5}$$

Multiple geometric dimensions for the model have been extracted from the literature. In addition, a CAD model, which itself was constructed from CT-scan images of a healthy human subject with no history of lower back pain was used for complementary geometric information [40].

Since the equations of motion were derived using bond graph modeling [41], it was necessary to obtain the relative velocities across force-generating elements, i.e., intervertebral discs and muscles. For this purpose, the velocity vectors of inertias on either side would first have to be transferred from the center of gravity to the disc interface and then projected along the disc's compliance directions. Since the inertias are modeled as rigid bodies with spatial dimensions, their velocity at the disc interface would be different from the velocity of their center of gravity. For instance, the lumbar vertebrae have a half-thickness distance in the tangential direction from their center of gravity to the disc interface, which contributes to changes in the vertebra's normal velocity at the disc interface as shown in Fig. 5 as D_B and D_T.

According to Fig. 5, velocity transfer from the vertebral center of gravity (CG) of each inertia to the top-bottom disc interface (TB) is given in Eq. (6):

$$\mathbf{V}_{\mathrm{i,TB}} = \mathbf{V}_{\mathrm{i,CG}} + \omega_{\mathrm{i}} \times \mathbf{D}_{\mathrm{i}} \rightarrow {V_{B,TB}}^n = {V_B}^n + D_B\omega_B \quad ; \quad {V_{T,TB}}^n = {V_T}^n - D_T\omega_T \tag{6}$$

Eq. (7) gives the interface velocities resolved into the compliance directions according to Fig. 4:

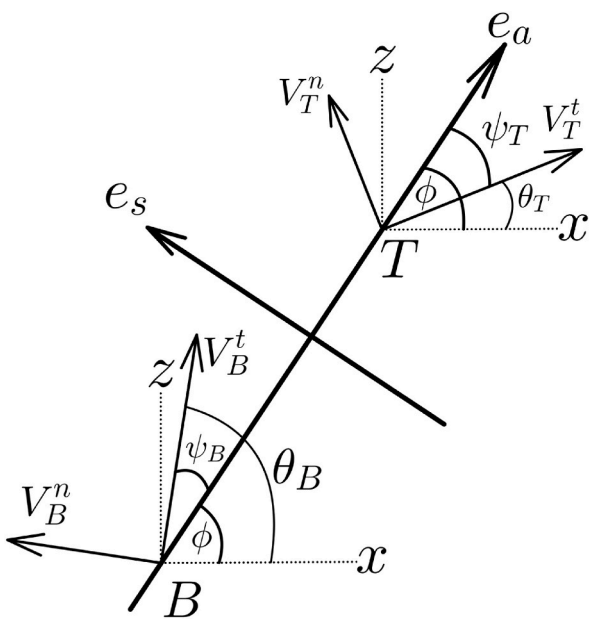

Fig. 4. Directions for axial and shear compliance.

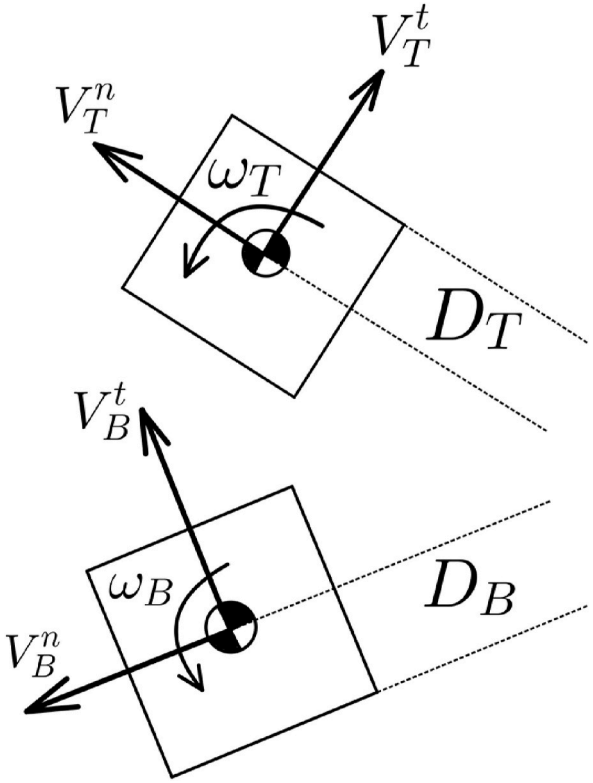

Fig. 5. Schematic of the half-thickness dimension used for velocity transfer in lumbar vertebrae.

$$\mathbf{V}_{\mathrm{i,TB}} = \left(V_i^t \cos\psi_i - V_{i,TB}{}^n \sin\psi_i\right)\mathbf{e_a} + \left(V_i^t \sin\psi_i + V_{i,TB}{}^n \cos\psi_i\right)\mathbf{e_s} \tag{7}$$

Eqs. (8) and (9) gives the relative velocity and relative angular velocity across intervertebral discs:

$$\mathbf{V}_{\mathrm{rel,TB}} = \mathbf{V}_{\mathrm{B,TB}} - \mathbf{V}_{\mathrm{T,TB}} = V_{\mathrm{rel,TB_a}}\mathbf{e_a} + V_{\mathrm{rel,TB_s}}\mathbf{e_s} \tag{8}$$

$$\omega_{TB} = \omega_B - \omega_T \tag{9}$$

where the relative velocity is considered positive in compression.

Another force-generating element that requires explanation is the musculature. There are a total of 6 muscles considered in the model: one global longissimus muscle that attaches the thorax to the pelvis, and five local multifidus muscles that attach the individual lumbar vertebrae to the pelvis. The location of the pelvic attachment point and the vertebral attachment points for each muscle are extracted from Arjmand et al. [42]. Fig. 6 shows a schematic of muscle architecture.

In Fig. 6, P and V denote pelvic and vertebral centers of gravity and p and v subscripts associate quantities with them, respectively. The angle α_i is the angle between the vertebral axis and the line that connects the vertebral center of gravity to the muscle attachment point. The length λ_i is the distance between the respective vertebral center of gravity and the muscle attachment point. Both α_i and λ_i are constants pertaining to each muscle and are obtained from the literature [40]. The angle ρ_i is defined in Eq. (10) as the difference between α_i and the individual inertia's orientation angle θ_i.

$$\rho_v = \alpha_v - \theta_v \quad \& \quad \rho_p = \alpha_p - \theta_p \tag{10}$$

Subsequently, the position of the muscle attachment point is calculated on both the pelvis (M_p) and the vertebra itself (M_v) in Eq. (11) and (12):

$$x_{M_i} = x_i + \lambda_i \cos\rho_i \tag{11}$$

$$z_{M_i} = z_i - \lambda_i \sin\rho_i \tag{12}$$

This enables the calculation of the muscle orientation angle δ and initial length L_0 in Eq. (13) and (14):

$$\delta = \tan^{-1}\frac{z_{M_v} - z_{M_p}}{x_{M_v} - x_{M_v}} \tag{13}$$

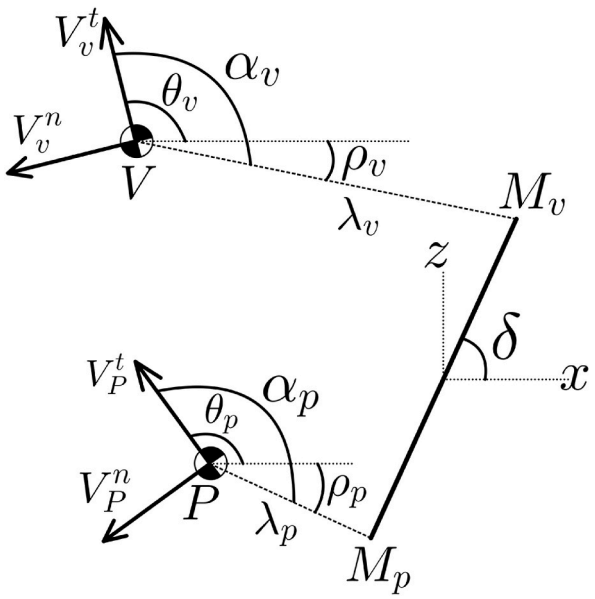

Fig. 6. Schematic of muscle architecture in the model.

$$L_0 = \left|\overline{M_v M_p}\right| = \sqrt{\left(z_{0M_v} - z_{0M_p}\right)^2 + \left(x_{0M_v} - x_{0M_v}\right)^2} \tag{14}$$

where L_0 is the initial, unstretched length of the muscle. To find the relative velocity across each muscle, the velocity of muscle attachment points for both the pelvis and the vertebra are calculated using velocity transfer in Eq. (15):

$$\mathbf{V}_{\mathrm{M}} = \mathbf{V}_{\mathrm{CG}} + \boldsymbol{\omega} \times \boldsymbol{\lambda} \tag{15}$$

Given that the muscle orientation is different than the body-fixed orientation for each vertebra, velocities are resolved in the inertial *x*-*z* frame (Fig. 2) with respective **i**, **k** unit vectors in Eq. (16):

$$\mathbf{V}_{\mathbf{M}} = (V_t \cos\theta - V_n \sin\theta + \lambda\omega \sin\rho)\mathbf{i} + (V_t \sin\theta + V_n \cos\theta + \lambda\omega \cos\rho)\mathbf{k} \tag{16}$$

Eq. (16) can be used to yield the velocity of both M_v and M_p muscle attachment points and Eq. (17) calculates the relative velocity across the muscle in the *x*–*z* frame, projected along the direction of the muscle itself which is determined by the muscle orientation angle δ.

$$\begin{aligned} \boldsymbol{V}_{\mathrm{rel},m} &= \boldsymbol{V}_{M_v} - \boldsymbol{V}_{M_p} = V_{\mathrm{rel},m_x}\boldsymbol{i} + V_{\mathrm{rel},m_z}\boldsymbol{k} \\ V_{\mathrm{rel},m} &= V_{\mathrm{rel},m_x}\, cos\ \delta + V_{\mathrm{rel},m_z}\, sin\ \delta \end{aligned} \tag{17}$$

where $V_{\mathrm{rel},m}$ is a scalar value that indicates the relative velocity across the muscle, considered positive in tension as muscles can only withstand tension [43].

2.4. Equations of motion and kinetics

Between any two inertias there is an axial compliance, a shear compliance, and a rotary compliance which exert forces and moments on said inertias. Furthermore, all inertias except that representing the head are subject to muscle forces which pull on them towards the pelvis. And finally, there are gravity forces acting vertically downward.

The described dynamics comprise a non-linear state space where the main state variables are the velocities of the inertias and the displacements across the compliances. Each inertia has three velocity states: tangential V_t, normal V_n, and angular ω and each compliance has three relative displacement states: axial q_a, shear q_s, and rotary q_r. Even though all energy elements (inertias, springs, and dampers) are considered to have linear constitutive behaviors, the dynamics are still non-linear, because of the system kinematics. Moreover, the state space is expanded to include auxiliary states which are not directly involved with storing or dissipating energy but are necessary for developing the dynamics. These auxiliary states consist of the angular and translational positions of the inertial elements.

The translational and rotary intervertebral compliance elements (TB) generate respective forces and moments given in Eqs. (18)–(20) that depend on the relative displacements and velocities across said elements, where the displacement is the temporal integral of said relative velocity.

$$\dot{q}_{TB_i} = V_{\mathrm{rel},TB_i} \quad ; \quad \dot{q}_{TB_r} = \omega_{\mathrm{rel},TB_r} \tag{18}$$

$$F^{i}_{TB} = k_{TB_i} q_{TB_i} + b_{TB_i} V_{\mathrm{rel},TB_i} \quad ; \quad M_{TB_r} = k_{TB_r} q_{TB_r} + b_{TB_r} \omega_{\mathrm{rel},TB_r} \tag{19}$$

Similarly, for the muscles:

$$\dot{q}_m = V_{\mathrm{rel},m} \quad ; F_m = k_m q_m + b_m V_{\mathrm{rel},m} \quad for\ q_m \geq 0 \tag{20}$$

The $q_m \geq 0$ condition ensures the muscle is in tension. In the equations above F denotes a force and M designates a moment. Also, k and b indicate linear stiffness and damping coefficients, the TB subscript indicates the top-bottom vertebral interface, and the m subscript pertains to a muscle. The i subscript indicates either of axial or shear, and the r subscript denotes rotation.

The acceleration vector in the rotating body-fixed frame is found via Eq. (21):

$$\mathbf{a} = \frac{\mathrm{d}\mathbf{V}}{\mathrm{d}t} = \frac{\partial \mathbf{V}}{\partial \mathrm{t}} + \boldsymbol{\omega} \times \mathbf{V} = (\dot{V}_t - \omega V_n)\mathbf{e_t} + (\dot{V}_n + \omega V_t)\mathbf{e_n} \tag{21}$$

where $\mathbf{e_t}$ and $\mathbf{e_n}$ are tangential and normal unit vectors, respectively.

Every force, including gravity, has to be resolved in tangential and normal directions and then their moment around the center of gravity needs to be calculated. Fig. 7 shows the direction of the gravity force in the body-fixed frame.

According to Fig. 7, the force of gravity is expressed as Eq. (22):

$$\mathbf{F_g} = mg(-\sin\theta \mathbf{e_t} - \cos\theta \mathbf{e_n}) \tag{22}$$

The force of gravity has no moment about the center of gravity.

As for the intervertebral compliance forces, according to the employed sign convention with relative velocity being positive in compression, a positive force pushes the top inertia up and the bottom inertia down, as shown in Fig. 8.

The intervertebral (TB) compliance forces are resolved in body-fixed directions in Eq. (23) and (24). For the top inertia:

$$\mathbf{F}_{\mathrm{TB,T}} = ({F_{TB}}^a \cos\psi_T - {F_{TB}}^s \sin\psi_T)\mathbf{e_t} + ({F_{TB}}^a \sin\psi_T + {F_{TB}}^s \cos\psi_T)\mathbf{e_n} \tag{23}$$

And for the bottom inertia:

$$\mathbf{F}_{\mathrm{TB,B}} = (-{F_{TB}}^a \cos\psi_B - {F_{TB}}^s \sin\psi_B)\mathbf{e_t} + ({F_{TB}}^a \sin\psi_B - {F_{TB}}^s \cos\psi_B)\mathbf{e_n} \tag{24}$$

Amongst intervertebral (TB) forces, the axial force generates no moment because it passes through the center of gravity. However, the shear force exerts a moment on each body due to the half-thickness distance between the disc interface and the vertebral center of gravity. Fig. 9 shows the orientation of the shear force with respect to the center of gravity.

According to Fig. 9, the shear force has a moment arm with respect to the centers of gravity denoted with l_i given in Eq. (25):

$$l_i = \frac{D_i}{\cos\psi_i} \tag{25}$$

The shear force's moment is then obtained via Eq. (26):

$${M_{s,TB}}^i = -{F_{TB}}^s l_i \tag{26}$$

It is noteworthy that the shear force opposes the rotation of both bodies.

With the relative muscle velocity being considered positive in tension, a positive muscle force pulls on both bodies along itself. Fig. 10 shows the orientation of the muscle force on the vertebra and its reaction on the pelvis with respect to the body-fixed coordinates.

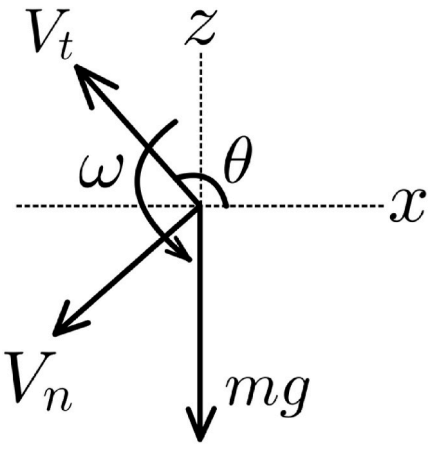

Fig. 7. Direction of the force of gravity in the body-fixed frame.

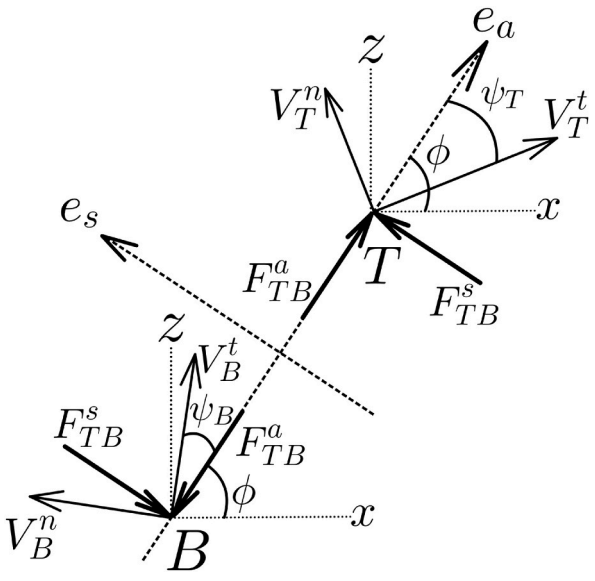

Fig. 8. Intervertebral (TB) forces in action and reaction.

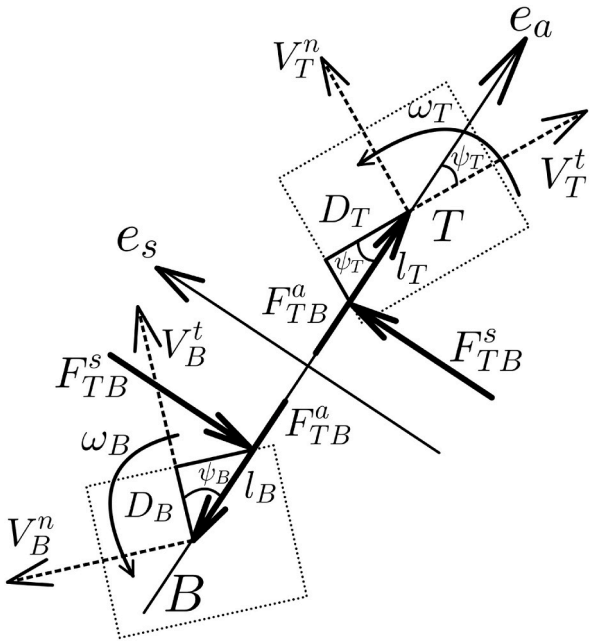

Fig. 9. Orientation of the intervertebral shear force with respect to centers of gravity.

The muscle force is expressed in body-fixed directions in Eqs. (27) and (28):

$$\mathbf{F}_{\mathrm{m_v}} = F_m(-\cos(\theta_v - \delta)\mathbf{e_t} + \sin(\theta_v - \delta)\mathbf{e_n}) = F_{m_{v_t}}\mathbf{e_t} + F_{m_{v_n}}\mathbf{e_n} \tag{27}$$

$$\mathbf{F}_{\mathrm{m_p}} = F_m\big(\cos\big(\theta_p - \delta\big)\mathbf{e_t} - \sin\big(\theta_p - \delta\big)\mathbf{e_n}\big) = F_{m_{p_t}}\mathbf{e_t} + F_{m_{p_n}}\mathbf{e_n} \tag{28}$$

The muscle force also produces a moment about the center of gravity for both the vertebra of interest and the pelvis. That moment is calculated via Eqs. (29) and (30) according to Fig. 10:

$$M_{m_v} = -\lambda_v F_m \cos\Big(\frac{\pi}{2} - (\rho_v + \delta)\Big) = -\lambda_v F_m \sin(\rho_v + \delta) \tag{29}$$

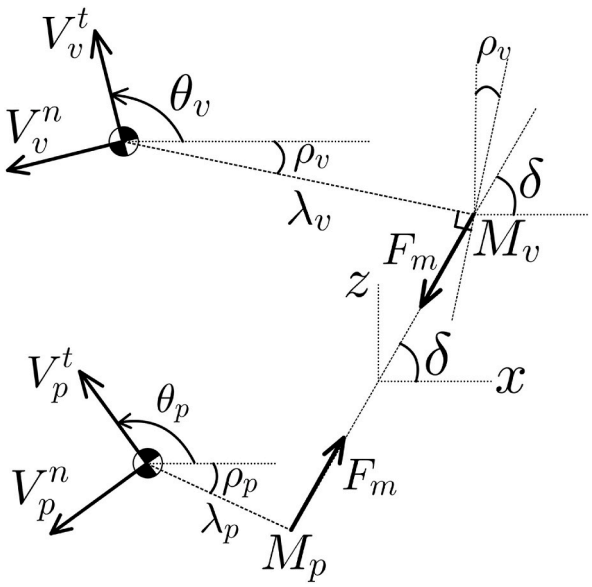

Fig. 10. Orientation of the muscle force.

$$M_{m_p} = \lambda_p F_m \cos\left(\frac{\pi}{2} - (\rho_p + \delta)\right) = \lambda_p F_m \sin(\rho_p + \delta) \tag{30}$$

The last forces that need attention are those from the seat. Fig. 11 schematically shows the orientation of the seat forces where H indicates the seat's base (hip cushion) and R_L, R_T denote the seat-contact point for the lumbar and thorax backrests, respectively. Also, d_L and d_H respectively indicate the distance between the lumbar and thorax backrest contact points and the seat's base. And β is the seat

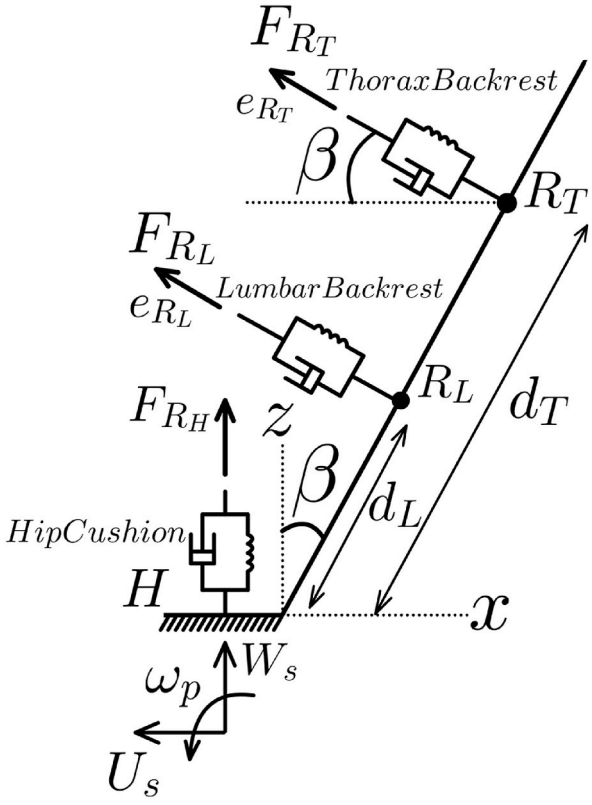

Fig. 11. Orientation of the seat forces.

backrest's inclination angle.

The seat forces can only push on the passenger's body which means their associated compliance can only undergo compression, i.e., $q_R \geq 0$. All seat compliances act only in one direction, perpendicular to the seat's orientation at the contact point. The hip cushion and its associated mass can only move vertically with respect to the vehicle as follows in Eq. (31):

$$\dot{q}_{R_H} = W_s - V_{\text{seat}_H} \;\; ; \;\; F_{R_H} = k_{R_H} q_{R_H} + b_{R_H}(W_s - V_{\text{seat}_H}) \quad for \;\; q_{R_H} \geq 0 \tag{31}$$

It is noted that F_{RH} does not generate any moment as the hip cushion's mass is considered to only move vertically.

To calculate the seat-backrest forces at either location, velocities of the two ends of the backrest compliance along its direction ($\mathbf{e_R}$) should be found. Eq. (32) gives the velocity transfer for the backrest contact point on the seat from the seat's base to the backrest's contact point as seen in Fig. 11, thus:

$$\mathbf{V_R} = \left(U_s \cos\beta + W_s \sin\beta + d_i \omega_p\right)\mathbf{e_R} \tag{32}$$

where the *i* subscript could be either L for the lumbar backrest or T for the thorax backrest. It is assumed that the seat backrest makes contact with the upper body at two points [21]: the lumbar backrest touches the lowest depression point on the lumbar spine at the spinous process of the L3 vertebra due to lordosis curvature, and the thorax backrest touches the highest protrusion point on the thoracic spine at the location of the spinous process of the T7 vertebra due to kyphosis curvature [26]. The dimensions of the vertebrae and the position vector that connects the inertia's center of gravity to the backrest contact point are extracted from the literature [31, 40].

Fig. 12 shows a schematic of the relative position of the seat backrest's contact point on the passenger body with respect to the associated inertia's center of gravity, where SP stands for spinous process and D_x and D_z are its distance from the vertebral center of gravity in inertial *x*–*z* directions.

The velocity of the spinous process is resolved in the backrest compliance's direction in Eq. (33):

$$\begin{aligned} \boldsymbol{V}_{\text{SP}} &= (V^t \, cos\,\theta - V^n \, sin\,\theta + \omega D_z)\boldsymbol{i} + (V^t \, sin\,\theta + V^n \, cos\,\theta + \omega D_x)\boldsymbol{k} \\ \boldsymbol{V}_{\text{SP}} &= V_{SP_x}\boldsymbol{i} + V_{SP_z}\boldsymbol{k} = \left(-V_{SP_x} \, sin\,\beta + V_{SP_z} \, cos\,\beta\right)\boldsymbol{e_R} \end{aligned} \tag{33}$$

Now the seat backrest (SBR) force along the compliance direction can be calculated via Eq. (34)

$$\mathbf{V}_{\text{rel}_{SBR}} = \mathbf{V}_{\text{R}} - \mathbf{V}_{\text{SP}} = V_{\text{rel}_{SBR}}\mathbf{e_R} \;\; ; \;\; \dot{q}_{SBR} = V_{\text{rel}_{SBR}} \;\; ; \;\; F_{SBR} = k_{SBR} q_{SBR} + b_{SBR} V_{\text{rel}_{SBR}} \tag{34}$$

From Fig. 12, the seat backrest force makes an angle equal to π-(β+θ) with respect to the tangential velocity of its associated inertia. Eq. (35) gives the seat backrest force and moment:

$$\begin{aligned} \boldsymbol{F}_{\text{SBR}} &= F_{SBR}(cos(\pi - (\theta + \beta))\boldsymbol{e_t} + sin(\pi - (\theta + \beta))\boldsymbol{e_n}) \\ M_{SBR} &= -D_z F_{SBR} \, cos\,\beta + D_x F_{SBR} \, sin\,\beta \end{aligned} \tag{35}$$

With all the acting forces and moments expressed in their respective body-fixed frames, the equations of motion are derived using Eq. (36)

$$m\dot{V}^t = m\omega V^n + \sum F_t \quad ; \quad m\dot{V}^n = -m\omega V^t + \sum F_n \quad ; \quad J\dot{\omega} = \sum M \tag{36}$$

The equations of motion are extensively given for the L3 vertebra as an example in Eq. (37) since its motion is relatively more involved as it experiences all the possible considered effects.

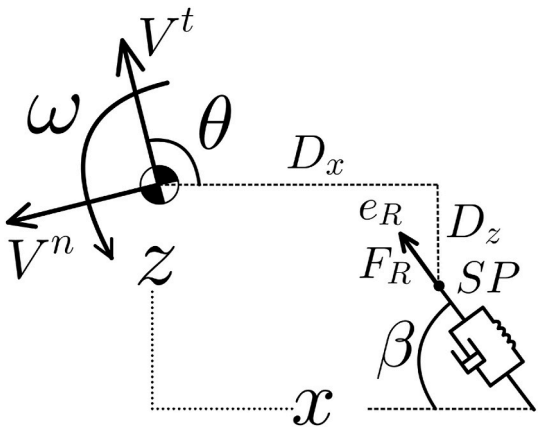

Fig. 12. The orientation of the backrest force with respect to the center of gravity of the associated inertia.

$$m_{L3}\dot{V}_{L3}{}^{t} = m_{L3}\omega_{L3}V_{L3}{}^{n} - m_{L3}g\sin\theta_{L3} + F_{L3L4}{}^{a}\cos\psi_{L3L4} - F_{L3L4}{}^{s}\sin\psi_{L3L4} - F_{L2L3}{}^{a}\cos\psi_{L3L2} - F_{L2L3}{}^{s}\sin\psi_{L3L2} - F_{SBR_{L3}}\cos(\theta_{L3}+\beta) + F_{m_{L3_t}}$$
$$m_{L3}\dot{V}_{L3}{}^{n} = -m_{L3}\omega_{L3}V_{L3}{}^{t} - m_{L3}g\cos\theta_{L3} + F_{L3L4}{}^{a}\sin\psi_{L3L4} + F_{L3L4}{}^{s}\cos\psi_{L3L4} + F_{L2L3}{}^{a}\sin\psi_{L3L2} - F_{L2L3}{}^{s}\cos\psi_{L3L2} + F_{SBR_{L3}}\sin(\theta_{L3}+\beta) + F_{m_{L3_n}}$$
$$J_{L3}\dot{\omega}_{L3} = M_{L3L4} - M_{L2L3} - M_{s_{L3L4}} - M_{s_{L2L3}} + M_{m_{L3}} + M_{SBR_{L3}} \tag{37}$$

2.5. Nonlinearity

The model is nonlinear as the equations of motion include nonlinear rotating frame cross product terms as well as many nonlinear trigonometric functions operating on the position states. Due to the inherent curvature in the geometry of the spine, excitation in one direction excites other directions as well, and thus the equations of motion for individual directions are coupled. The trigonometric nonlinearities are an intrinsic characteristic of the model's geometry, and the motion of the associated angles is sufficiently large that these trigonometric functions are retained. This is in particular because of the use of the arctangent function that is employed to calculate the φ angles that determine the instantaneous orientation of the intervertebral compliances (Eq. (4)). The arctangent function cannot be approximated by a linear term for the purpose of the calculations in this model, as its series approximation diverges for tangent values with magnitudes greater than 1 and the φ angles here typically range between 75 and 125° whose tangents have magnitudes much larger than 1. Furthermore, retaining the nonlinear terms enables the application of this model for analyzing large-displacement motions as well as small displacements, should proper viscoelastic properties be available.

2.6. Initial conditions

Each state requires an initial condition value. The initial condition for the auxiliary states, including translational and angular positions of the inertias, is extracted from the literature [31,40]. The velocity states all have zero initial conditions. However, since the model is subject to gravity, the displacement states have non-zero initial conditions. Given how the equations of motion are heavily coupled, an analytic derivation of those initial conditions was not performed. Instead, the model was run with zero initial conditions and zero inputs, and the system was allowed to settle into a static equilibrium. The resulting displacement states were then saved as the initial conditions for ensuing runs of the model.

2.7. Parameter investigation

There are quite a few parameters employed in developing the model. They include stiffness and damping coefficients associated with eight intervertebral compliances in three directions, stiffness and damping coefficients for the six modeled muscles, mass and moments of inertia for eight inertial elements (pelvis, five lumbar vertebrae, thorax, head), and a mass, stiffness, and damping coefficients associated with the seat. This adds up to a total of 79 parameters.

While the fundamental dynamics depend on the modeling assumptions, the response-time history, and the associated critical frequencies greatly depend on the parameter values. Parameters have been extracted from the literature as best as possible. Finding the required parameters within the literature proved a challenge as no unique study has reported all 79 required parameters in the way identified in this study. Hence, the parameters needed to be extracted from various studies where differing experimental methods were used to obtain said parameters, and therefore there is not total agreement among researchers. For this reason, it was necessary to adapt some of the employed parameters to match experimental results. This was achieved through a numerical optimization where important parameters were identified and varied within a range to arrive at a set of parameters that could replicate experimental data with sufficient accuracy.

Among the various parameter groups, the highest level of confidence belongs to masses and moments of inertia. These inertial parameters are the same for a living person and a cadaver and have been studied extensively in anthropometry studies, and multiple highly-cited references have reported similar values for the masses and moments of inertia [44,45]. Therefore, the inertial parameters were not considered in the parameter optimization and they have been utilized in the model as given by the literature [31,46].

It was found that the vibration transmissibility was most affected by the intervertebral translational stiffness and damping coefficients, respectively. Stiffness parameters do not come with the same level of confidence as the inertial parameters, as most experiments that give values for stiffness are performed on cadavers, and the force-generation mechanism for a living organism is not the same as a cadaver. Lastly, the least level of confidence belongs to the damping parameters, which add time-dependence to the force-generation mechanism as well. Quite a few references were investigated to obtain the required stiffness and damping parameters, including but not limited to Refs. [22–25,27,44,45]. It was observed that they did not agree on the lumping strategy for defining the parameters or on the parameter values themselves. In some cases, they differed by an order of magnitude.

Consequently, some biomechanical parameters, particularly the damping values, had to be modified from their initial values extracted from the literature to enable model validation against experimental findings. The initial values for the biomechanical stiffness parameters were taken from Keller et al. [47]. Stiffness values were proportionally varied from Keller et al.'s initial guess, and a varying damping ratio was applied to calculate an average damping coefficient for each intervertebral, translational damper element according to the stiffness of the spring next to it and the masses on either side as follows in Eq. (38):

$$k_{TBa,s} = \eta k_{TBa,s\,Keller} \quad ; \quad b_{TBa,s} = 2\zeta\sqrt{k_{TBa,s}\frac{m_T + m_B}{2}} \tag{38}$$

where η is the proportionality constant between the used stiffness values and the same values from Keller et al., which was found to be 36% and 49% for the axial direction and the shear direction, respectively. Also ζ is the employed damping ratio which was found to be 0.5. This set of parameters was able to replicate experimental results with reasonable accuracy and was chosen accordingly.

Additionally, seat parameters were taken from Papaioannou et al. [46]. For the muscles, Young's modulus E_m, damping ratio ζ_m, and cross-sectional area A_m were extracted from the literature, respectively [48–50], and the muscle stiffness and damping coefficients were calculated as follows via Eq. (39):

$$k_m = \frac{E_m A_m}{L_0} \quad ; \quad b_m = 2\zeta_m \sqrt{k_m m_v} \tag{39}$$

where L_0 is the muscle's unstretched length, and m_v is the mass of the vertebral body to which the muscle is attached. The parameters employed in this study are given in Tables 1–12.

3. Validation

Before the model can be used to make further inferences on the internal motions within the body, it needs to be validated, i.e., assert that it can predict reasonable outputs according to the available literature. The present model has been validated against Pranesh et al. [33]. In their study, 12 seated human subjects with no history of lower-back pain were exposed to vibrations of vehicular nature with vertical excitations at the base. Using accelerometers, vibration transmissibility frequency responses were recorded at different locations of the upper body. Fig. 13 compares the vibration transmissibility as predicted by the model here with the experimental data from Pranesh et al. Given that vertical vibrations are responsible for the majority of the perception of ride comfort, vertical vibration transmissibility is compared to Pranesh's experiment in three different locations: the L5 and L3 vertebra within the lumbar spine, and the head at the top of the model. Fig. 13(a) through (c) show this comparison. Also, the horizontal vibration transmissibility in response to the same vertical excitation at the base is investigated for the head in Fig. 13(d) to account for the fore-aft degree of freedom.

As seen in Fig. 13, the results from Pranesh et al. have a noticeable variability. This is due to how the different human subjects in their experiment must have had different bodily constitutions, and while their response is similar in shape, they are not exactly the same for every subject. Fig. 13 shows that the model developed here agrees sufficiently well with Pranesh et al. in both magnitude and frequency content.

To quantify the accuracy of the validation, first an average experimental curve was required to represent Pranesh et al.'s data. For this purpose, curves were fit ($R^2 = 99\%$) to the bulk of Pranesh's data to represent the average experimental data for vibration transmissibility. Fig. 14(a) through (d) show how the model compares against Pranesh et al.'s average response.

Fig. 14 suggests that the model replicates Pranesh's experimental results with sufficient accuracy. To quantify this accuracy, however, a frequency-averaged, relative error is defined in Eq. (40) as a measure of the deviation of the model from Pranesh's experiment:

Table 1
Inertial parameters for the passenger model from [31,51].

Level	Mass – m (kg)	Sagittal Mass Moment of Inertia – I_{yy} (×10^−4 kg m^2)
Pelvis	8.1541	300
L5	2.1243	54.6
L4	2.0367	52.0
L3	1.9710	54.1
L2	1.8907	59.1
L1	1.8250	64.0
Thorax	16.0746	1250
Head	5.0662	293.4

Table 2
Translational Intervertebral Stiffness Values, initial guess from Ref. [47], modified to match [33].

Section	Initial k_a (kN/m)	Modified k_a (kN/m)	Initial k_s (kN/m)	Modified k_s (kN/m)
Pelvis-Seat	300	108	200	98
L5S1	510	184	45	22.1
L4L5	450	162	30	14.7
L3L4	525	189	30	14.7
L2L3	600	216	35	17.6
L1L2	620	223.2	40	19.6
T-L1	640	230.4	50	24.5
Neck	1250	450	30	14.7

Table 3
Translational Intervertebral Damping Values, initial guess from Ref. [51], modified to match [33].

Section	Initial b_a (Ns/m)	Modified b_a (Ns/m)	Initial b_s (Ns/m)	Modified b_s (Ns/m)
Pelvis-Seat	1200	938	1200	894
L5S1	1200	971	1200	337
L4L5	1200	581	1200	175
L3L4	1200	615	1200	172
L2L3	1200	646	1200	182
L1L2	1200	644	1200	191
T-L1	1200	1436	1200	468
Neck	1200	2181	1200	394

Table 4
Rotational intervertebral stiffness and damping values, from [47,51].

Section	k_r (Nm/rad)	b_r (Nms/rad)
Pelvis-Seat	700	1.2
L5S1	75	1.2
L4L5	80	1.2
L3L4	100	1.2
L2L3	120	1.2
L1L2	140	1.2
T-L1	160	1.2
Neck	400	1.2

Table 5
Seat parameters, from [46].

Mass – m_{seat} (kg)	Cushion Stiffness – k_{seat} (kN/m)	Cushion Damping – b_{seat} (Ns/m)
13.6	80	1350

Table 6
Muscle material properties, from [48,49].

Muscle	Young's Modulus – E_m (kPa)	Damping Ratio – ζ_m
Multifidus	91.34	0.58
Longissimus	62.85	0.58

Table 7
Associated muscles' geometric parameters, from [42,50].

	Thorax	L1	L2	L3	L4	L5
Initial Length – L0 (cm)	26.57	14.03	11.59	9.14	7.11	4.81
Cross Sectional Area – A_m (cm^2)	18.5	1.95	3.18	4.74	6.50	7.14

$$\varepsilon = \sqrt{\frac{\int_{f_0}^{f_\infty} \left(\frac{Trm - Trm_{Pranesh}}{Trm_{Pranesh}} \right)^2 df}{f_\infty - f_0}} \tag{40}$$

where *Trm* denotes transmissibility. The bounds of the frequency range of interest are selected to be $f_0 = 0.5$ Hz and $f_\infty = 20$ Hz. The frequency-averaged, relative error ε was calculated to be 6%, 6%, 5%, and 7% for L5 vertical, L3 vertical, head vertical, and head horizontal transmissibilities, respectively.

This provides some confidence that this model can predict reasonably accurate results and could be further employed to make inferences regarding the body's internal dynamics. It is also noteworthy that Figs. 13–14(c) and (d) display the vertical and horizontal seat-to-head transmissibility (STHT), which is one of the commonly recognized biodynamic characteristics in biomechanical modeling of seated humans.

4. Results and discussion

The model's response has been simulated using MATLAB SIMULINK®. Fig. 15 shows the axial displacement deviation at various vertical locations for a unit heave-impulse at the base of the model.

Table 8
Geometric Parameters for Muscle Attachment Points on both Vertebra and Pelvis [40].

		Thorax	L1	L2	L3	L4	L5
On Vertebra	α_v (deg)	171.2	89.8	89.6	101.9	108.1	105.2
	λ_v (mm)	178.3	68.8	66.8	72.6	68.6	63.3
On Pelvis	α_p (deg)	178.1	150.5	158.0	165.9	164.9	164.8
	λ_p (mm)	44.2	46.9	51.1	61.2	65.2	67.3

Table 9
Geometric parameters for seat backrest contact points [40].

	Distance to base – d (mm)	x-Distance to CG – D_x (mm)	z-Distance to CG – D_z (mm)
Lumbar Contact Point	212.5	69.9	19.3
Thorax Contact Point	438.9	64.8	66.8

Table 10
Tangential half-thickness dimensions for velocity transfer [40].

Level	Head-Thorax	L1	L2	L3	L4	L5	Pelvis-L5
Half-Thickness (mm)	121.4	13.8	14.5	14.6	15.1	13.9	37.5

Table 11
Distance from CG to compliance interface [40].

	Pelvis-Seat (tangential)	Pelvis-Seat (normal)	Thorax-L1 (tangential)	Thorax-L1 (normal)	Thorax-Head (tangential)	Thorax-Head (normal)
Distance (mm)	−89.8	65.3	−164.9	67.4	265.1	−19.6

Table 12
Geometric initial conditions with seat base at the coordinate origin [40].

	Head	Thorax	L1	L2	L3	L4	L5	Pelvis
Initial Angle θ_0 (deg)	75.6	104.0	65.9	71.3	83.9	98.8	107.6	135.0
Initial Position x (mm)	−55.9	−10.7	−45.4	−58.4	−63.8	−61.4	−50.5	−17.3
Initial Position z (mm)	767.7	505.7	308.4	271.0	231.8	192.0	155.8	109.6

Fig. 15 shows that, in those sections that are closer to the base, the effect of the input is noticed both earlier and with higher intensity, such that a wave-like behavior is observed in the propagation of the excitation motion within the passenger's body.

Another subject of interest is the model's frequency response. The non-linear model has been linearized around its equilibrium, and its frequency response has been investigated. To ascertain the accuracy of the linearization, the non-linear model was simulated for a small-amplitude harmonic input with a frequency sweep in the range of interest. It was determined that the linearized frequency response was virtually identical to the small-input, non-linear response. Frequency response plots were generated for various intersegmental velocity responses against the three heave, cruise, and pitch input velocities for a frequency range of 0.1–20 Hz. This range encompasses the entire range of vibration signals coming from a generic vehicle, which is about 1–10 Hz [52]. It is noteworthy that this frequency response is identical to that of one between respective intersegmental displacements and input displacements, since velocity and displacement are proportional in the frequency domain, as shown in Eq. (41):

$$\frac{V_{rel}(s)}{V_{in}(s)} = \frac{\mathscr{L}(\dot{q})}{\mathscr{L}(\dot{q}_{in})} = \frac{sq(s)}{sq_{in}(s)} = \frac{q(s)}{q_{in}(s)} \tag{41}$$

Fig. 16 shows the non-dimensional vibration transmissibility for axial and shear motions subject to translational excitation velocities at three joint locations: the L5S1 and L4L5 lumbar discs at the bottom and the neck at the top of the model.

Fig. 16(a) shows that in response to vertical excitation, it is the L4L5 disc that experiences the highest vibration transmissibility for axial displacement, with L5S1 being a close second. However, for shear displacement due to heave input, it is L5S1 that sees the highest transmissibility, as evident in Fig. 16(c). This corroborates with L5S1's inherent slanted orientation, where its askew geometry induces a substantial shear force when exposed to vertical excitation [26]. Similarly, said slanted geometry causes the same cross-transmission effect as noted in Fig. 16(b), where L5S1 experiences a higher transmissibility for axial displacement when subject to a horizontal excitation. Fig. 16(a) through (c) correspond well with how most chronic lower back pain is associated with the lower lumbar region [28], as the L4L5 and L5S1 discs have developed the highest translational transmissibility. The smallest translational transmissibility is generally observed at the level of the neck. However, as depicted in Fig. 16(d), the neck experiences the highest transmissibility in shear vibrations when exposed to horizontal excitations within the vehicular frequency range of interest. This corresponds with how

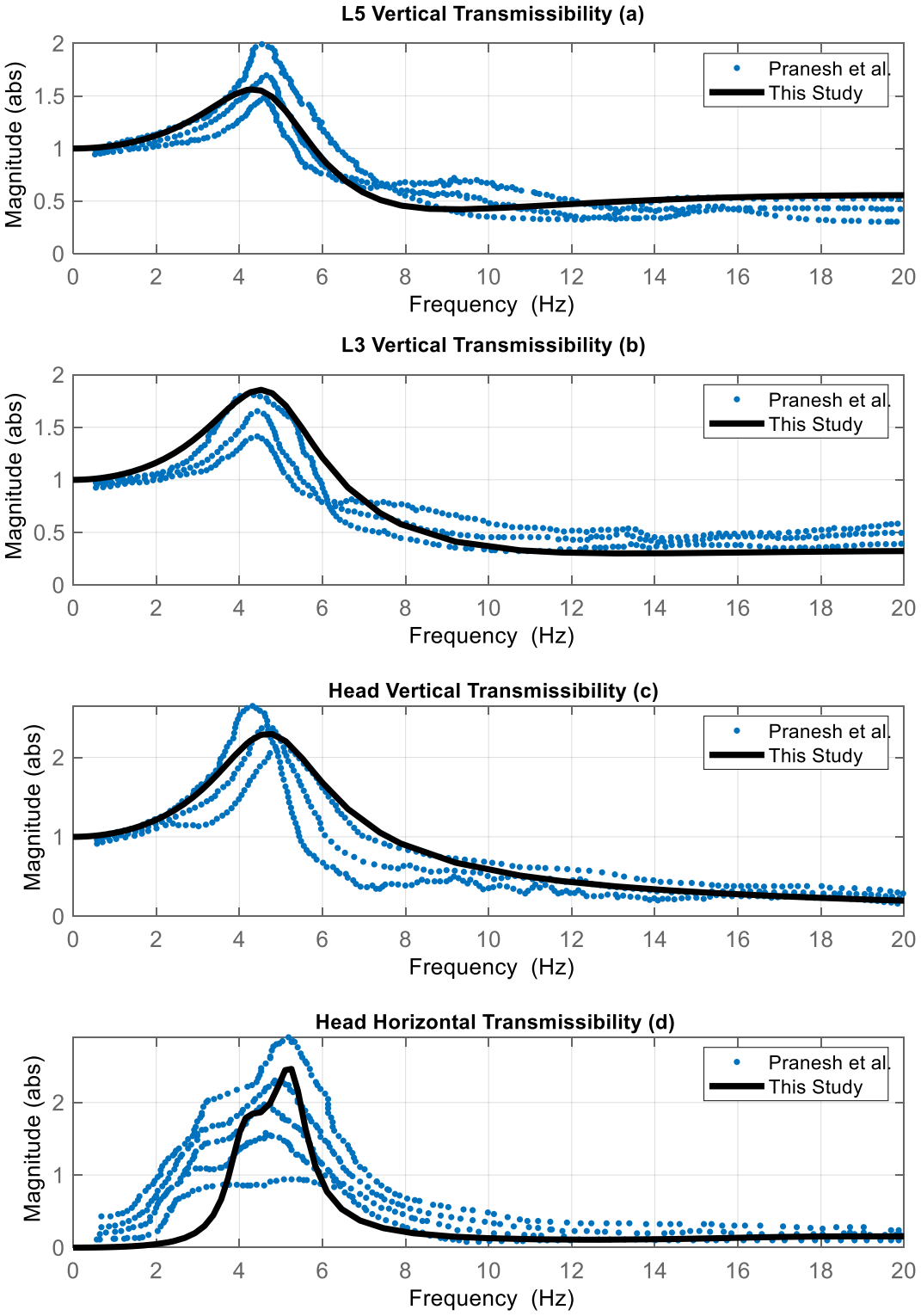

Fig. 13. Comparison of vibration transmissibility between this study and Pranesh et al.'s experiment [33] (a) L5 vertebra, vertical. (b) L3 vertebra, vertical. (c) Head, vertical. (d) Head, horizontal.

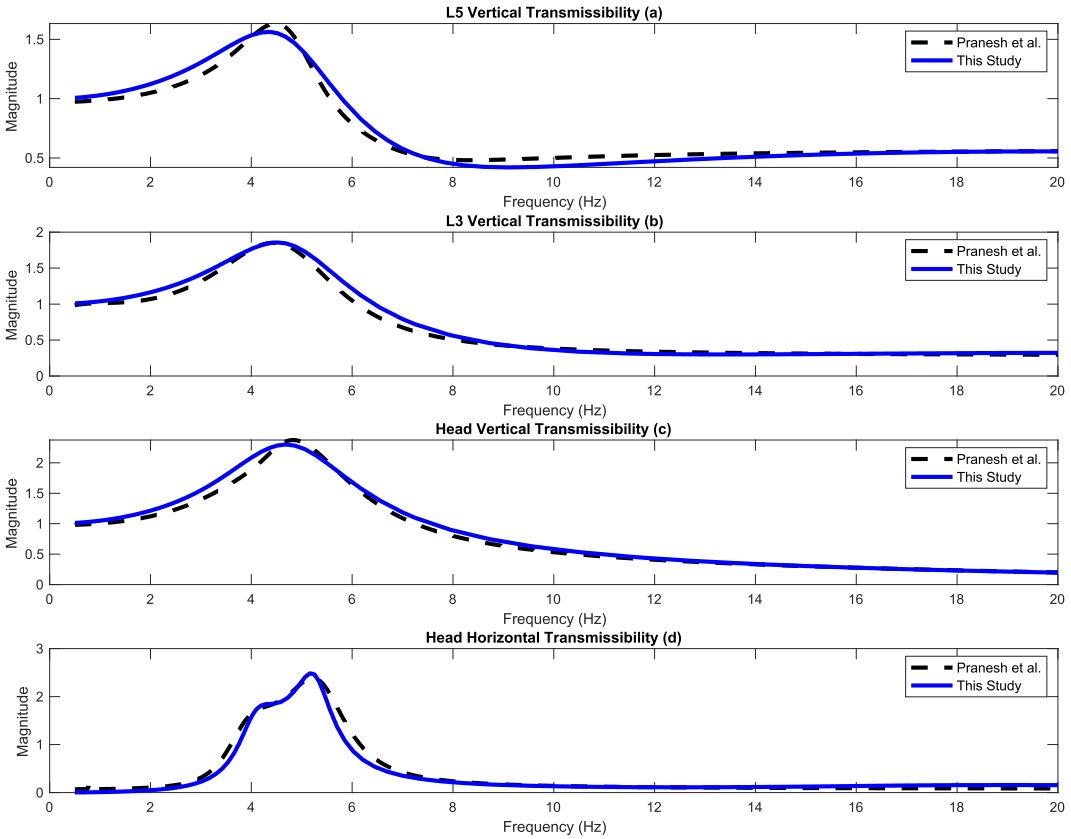

Fig. 14. Comparison of vibration transmissibility between this study and Pranesh et al.'s average response [33] (a) L5 vertebra, vertical. (b) L3 vertebra, vertical. (c) Head, vertical. (d) Head, horizontal.

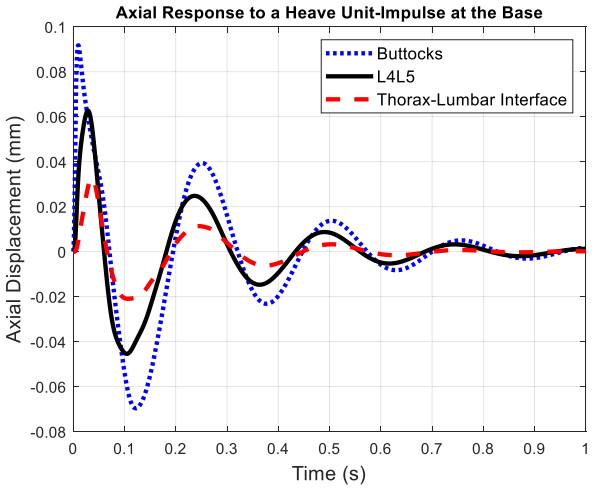

Fig. 15. Wave-like propagation of an impulse within various sections of the model.

the majority of neck injuries are shear-related and are commonly associated with head-on collisions [53]. Fig. 17 depicts the non-dimensional rotational frequency response for a rotary excitation.

Fig. 17 shows that the neck has the highest rotational susceptibility to rotary excitation for the vehicular frequency range. Fig. 18 extensively investigates the non-dimensional translational transmissibility for translational excitations for the L4L5 disc.

Fig. 18 (a) and (b) show that in response to both translational inputs, the shear displacement has a higher transmissibility than that of axial displacement for all frequencies. Fig. 18(c) and (d) show that within the frequency range of interest, both translational

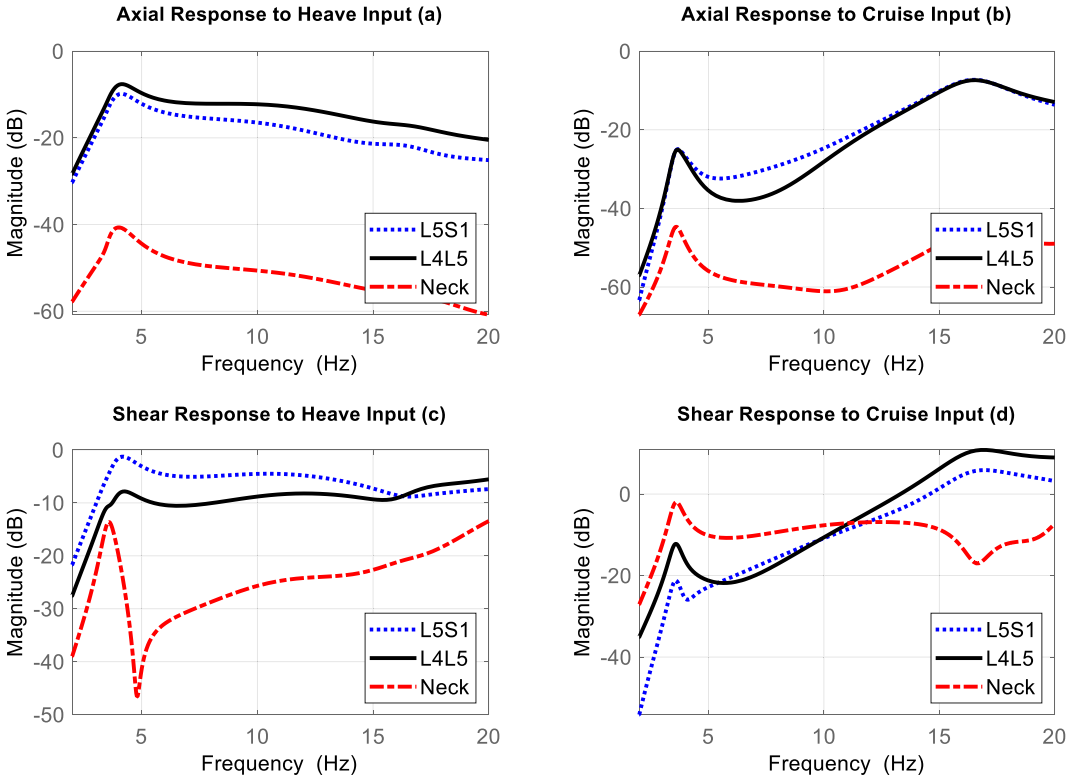

Fig. 16. Translational Frequency Responses for L5S1, L4L5, and Neck Joints (a) axial vs. heave. (b) Axial vs. cruise. (c) Shear vs. heave. (d) Shear vs. cruise.

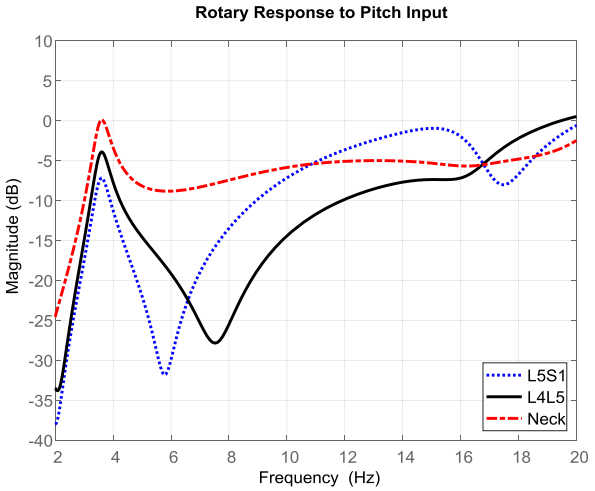

Fig. 17. Rotary frequency response for the L5S1, L4L5, and neck joints.

responses are more susceptible to the heave input despite the cruise input taking over at higher frequencies. It can also be noted in Fig. 18 that vibration is reduced in all cases except for the shear displacement in response to cruise input that gets some amplification at higher frequencies.

Another noteworthy remark that can be observed from all frequency responses is that vibration transmission has a peak at around 4.5 Hz for all displacements and excitations. This is noticed in Pranesh's experiment [33] too, and indicates a resonant natural frequency of about 4.5 Hz that falls within the vehicular frequency range. It also corresponds to the findings from other biomechanical models that have observed a fundamental natural frequency of about 4.5 Hz for human body vibration, including Guruguntla and Lal [20], Liang and Chiang [23], Kim et al. [24], and Cho and Yoon [21].

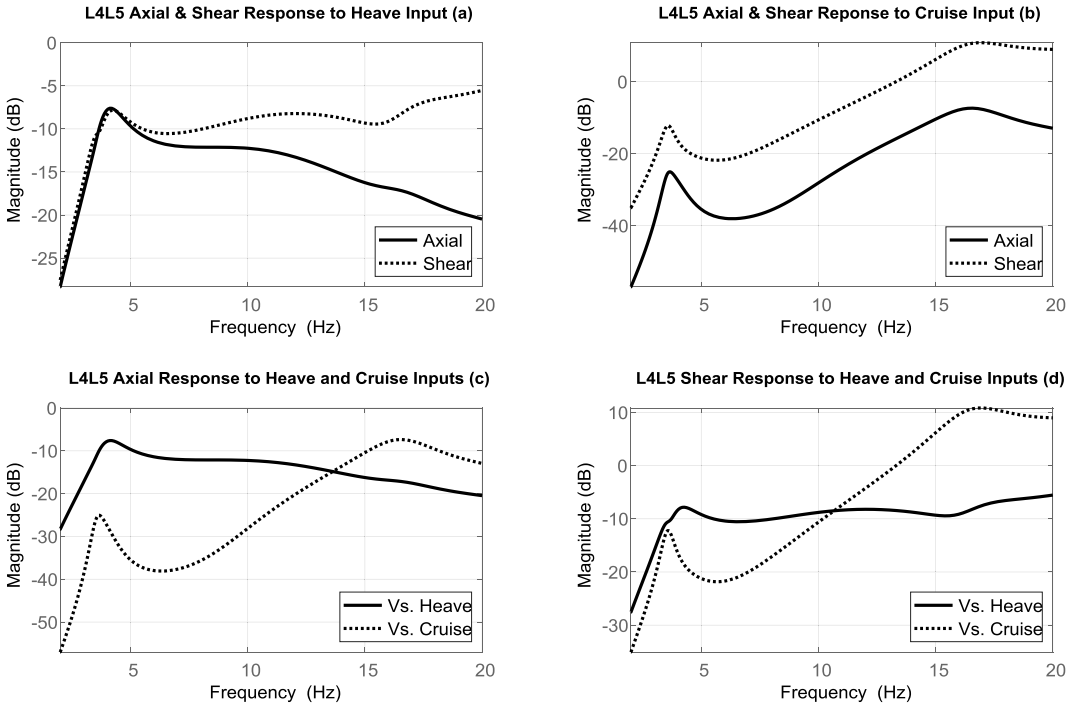

Fig. 18. Comparing translational Frequency Responses of the L4L5 Joint (a) axial and shear vs. heave. (b) Axial and shear vs. cruise. (c) Axial vs. heave and cruise. (d) Shear vs. heave and cruise.

The main advantage of this research is enabling curved motion and tracking smooth trajectories through the use of a few simple geometric assumptions, thus providing an intuitive, sufficiently accurate, low-order model. This allows for smoother posture prediction.

Furthermore, because of how the model employs much fewer degrees of freedom than finite element studies, it is computationally lighter and more time-efficient.

Another advantage of this study is that it readily yields the spinal loads that are known to cause discomfort or injury, as the presented model studies the lumbar spine extensively. This enables the application of the model in injury estimation [14], ergonomics studies [15], and rehabilitation [16].

The main limitation of this study is that its application is restricted to small-amplitude motions, as the force-generating elements generally display nonlinear behaviors for large displacements. However, due to the inclusion of geometric nonlinearities, its application can readily be extended to large-amplitude motions by introducing proper stiffness and damping characteristics.

Another reservation is that this model has excluded the arms and therefore cannot thoroughly account for the case of a driver with hands on the steering wheel, where the dynamic response is somewhat different according to Ref. [33]. A final remark is that this study has considered motions in the sagittal plane to be decoupled from other anatomical planes. While in general there is some degree of coupling amongst motions within said planes, Russell et al. have argued that sagittal motions are dominated by sagittal actions [54]. Hence, considering sagittal actions should suffice for adequately predicting sagittal motions.

5. Conclusion

A nonlinear biomechanical model of the upper body was developed for the purpose of studying the propagation of disturbance inputs from a generic vehicle to a seated passenger. The model replicates experimental data with sufficient accuracy and fidelity. The proposed model accounts for curved motion and allows for the prediction of all small-amplitude sagittal motions. This model employs much fewer degrees of freedom than similar finite element models and is therefore computationally lighter and provides additional geometric and analytical intuition into the upper body's internal dynamics. Upon simulation of frequency response, it was shown that within the vehicular frequency range of 1–10 Hz, the lower lumbar region, namely the L5S1 and L4L5 discs, experience the highest translational vibration transmissibility and the neck experiences the highest rotational vibration transmissibility. The model suggests that the maximum vibration transmissibility occurs at about 4.5 Hz. This signifies a fundamental natural frequency of the human body and could be the designated frequency for vibration mitigation and controller design. The model can be employed in ride-comfort studies and help define a quantitative ride-comfort index, such that the most comfortable ride would be one that has induced the least internal displacements. Also, the model has applications in any other study that might require an assessment of the internal dynamics of the upper body.

Ethics declaration

Informed consent was not required for this study because no human subject experiments or surveys were involved and experimental results needed for validation were directly extracted from globally published work.

CRediT authorship contribution statement

Ali Akbari: Writing – original draft, Visualization, Validation, Software, Resources, Project administration, Methodology, Investigation, Formal analysis, Data curation, Conceptualization. **Donald Margolis:** Writing – review & editing, Supervision, Funding acquisition.

Declaration of competing interest

The authors declare that they have no known competing financial interests or personal relationships that could have appeared to influence the work reported in this paper.

References

[1] C. Wang, X. Zhao, R. Fu, Z. Li, Research on the comfort of vehicle passengers considering the vehicle motion state and passenger physiological characteristics: improving the passenger comfort of autonomous vehicles, Int. J. Environ. Res. Publ. Health 17 (2020) 6821, https://doi.org/10.3390/ijerph17186821.
[2] M.G. Da Silva, Measurements of comfort in vehicles, Meas. Sci. Technol. 13 (2002) R41, https://doi.org/10.1088/0957-0233/13/6/201.
[3] D. Oborne, Whole-body vibration and international standard ISO 2631: a critique, Hum. Factors 25 (1983) 55–69.
[4] P. Els, The applicability of ride comfort standards to off-road vehicles, J. Terramechanics 42 (2005) 47–64, https://doi.org/10.1016/j.jterra.2004.08.001.
[5] Y. Yang, W. Ren, L. Chen, M. Jiang, Y. Yang, Study on ride comfort of tractor with tandem suspension based on multi-body system dynamics, Appl. Math. Model. 33 (2009) 11–33, https://doi.org/10.1016/j.apm.2007.10.011.
[6] D. Oborne, Vibration and passenger comfort, Appl. Ergon. 8 (1977) 97–101.
[7] K.C. Parsons, E.M. Whitham, M.J. Griffin, Six axis vehicle vibration and its effects on comfort, Ergonomics 22 (1979) 211–225, https://doi.org/10.1080/00140137908924605.
[8] H. Hayati, D. Eager, A.-M. Pendrill, H. Alberg, Jerk within the context of science and engineering—a systematic review, Vibration 3 (2020) 371–409, https://doi.org/10.3390/vibration3040025.
[9] ISO, Shock evaluation of human exposure to whole-body vibration, in: ISO 2631, International Organization for Standardization, 1997.
[10] B. Khorram, A. Wåhlberg, A. Tavakoli Kashani, Longitudinal jerk and celeration as measures of safety in bus rapid transit drivers in Tehran, Theor, Issues Ergon. Sci. 21 (2020) 577–594, https://doi.org/10.1080/1463922X.2020.1719228.
[11] M. Fard, L. Lo, A. Subic, R. Jazar, Effects of seat structural dynamics on current ride comfort criteria, Ergonomics 57 (2014) 1549–1561, https://doi.org/10.1080/00140139.2014.934300.
[12] BSI, Guide to Measurement and Evaluation of Human Exposure to Whole-Body Mechanical Vibration and Repeated Shock, BS6841, British Standards Institution, 1987.
[13] VDI, Human exposure to mechanical whole-body vibration, in: VDI2057, Association of German Engineers, 2002.
[14] K.-U. Schmitt, P.F. Niederer, D.S. Cronin, B. Morrison III, M.H. Muser, F. Walz, Trauma Biomechanics: an Introduction to Injury Biomechanics, Springer, 2019.
[15] S.M. McGill, Evolving ergonomics? Ergonomics 52 (2009) 80–86, https://doi.org/10.1080/00140130802480851.
[16] D.A. Neumann, Kinesiology of the Musculoskeletal System-E-Book: Foundations for Rehabilitation, Elsevier Health Sciences, 2016.
[17] M. Gohari, M. Tahmasebi, Active off-road seat suspension system using intelligent active force control, J. Low Freq. Noise Vib. Act. Control 34 (2015) 475–489.
[18] A. Kuznetsov, M. Mammadov, I. Sultan, E. Hajilarov, Optimization of a quarter-car suspension model coupled with the driver biomechanical effects, J. Sound Vib. 330 (2011) 2937–2946, https://doi.org/10.1016/j.jsv.2010.12.027.
[19] R.-c. Dong, L. He, W. Du, Z.-k. Cao, Z.-l. Huang, Effect of sitting posture and seat on biodynamic responses of internal human body simulated by finite element modeling of body-seat system, J. Sound Vib. 438 (2019) 543–554, https://doi.org/10.1016/j.jsv.2018.09.012.
[20] V. Guruguntla, M. Lal, An improved biomechanical model to optimize biodynamic responses under vibrating medium, J. Vib. Eng. Technol. 9 (2021) 675–685, https://doi.org/10.1007/s42417-020-00254-x.
[21] Y. Cho, Y.-S. Yoon, Biomechanical model of human on seat with backrest for evaluating ride quality, Int. J. Ind. Ergon. 27 (2001) 331–345, https://doi.org/10.1016/S0169-8141(00)00061-5.
[22] N. Mohajer, H. Abdi, S. Nahavandi, K. Nelson, Directional and sectional ride comfort estimation using an integrated human biomechanical-seat foam model, J. Sound Vib. 403 (2017) 38–58, https://doi.org/10.1016/j.jsv.2017.05.019.
[23] C.-C. Liang, C.-F. Chiang, Modeling of a seated human body exposed to vertical vibrations in various automotive postures, Ind. Health 46 (2008) 125–137, https://doi.org/10.2486/indhealth.46.125.
[24] T.-H. Kim, Y.-T. Kim, Y.-S. Yoon, Development of a biomechanical model of the human body in a sitting posture with vibration transmissibility in the vertical direction, Int. J. Ind. Ergon. 35 (2005) 817–829, https://doi.org/10.1016/j.ergon.2005.01.013.
[25] Y. Kozawa, G. Sugimoto, Y. Suzuki, A new ride comfort meter, SAE Trans. (1986) 1038–1045.
[26] J.A. Ashton-Miller, A.B. Schultz, Biomechanics of the human spine, Basic Orthopaed. Biomech. 2 (1997) 353–385.
[27] RadiologyKey.com, Figure 9.1: Sagittal View of the Spine Showing Vertebral Levels, 2016. https://radiologykey.com/spine-5/.
[28] J.N. Katz, Lumbar disc disorders and low-back pain: socioeconomic factors and consequences, JBJS 88 (2006) 21–24, https://doi.org/10.2106/JBJS.E.01273.
[29] T. Keller, Z. Mao, D. Spengler, Young's modulus, bending strength, and tissue physical properties of human compact bone, J. Orthop. Res. 8 (1990) 592–603, https://doi.org/10.1002/jor.1100080416.
[30] D. Morita, Y. Yukawa, H. Nakashima, K. Ito, G. Yoshida, M. Machino, S. Kanbara, T. Iwase, F. Kato, Range of motion of thoracic spine in sagittal plane, Eur. Spine J. 23 (2014) 673–678, https://doi.org/10.1007/s00586-013-3088-7.
[31] D.J. Pearsall, J.G. Reid, L.A. Livingston, Segmental inertial parameters of the human trunk as determined from computed tomography, Ann. Biomed. Eng. 24 (1996) 198–210, https://doi.org/10.1007/BF02667349.
[32] S.M. McGill, S. Grenier, N. Kavcic, J. Cholewicki, Coordination of muscle activity to assure stability of the lumbar spine, J. Electromyogr. Kinesiol. 13 (2003) 353–359, https://doi.org/10.1016/S1050-6411(03)00043-9.
[33] A. M-Pranesh, S. Rakheja, R. Demont, Influence of support conditions on vertical whole-body vibration of the seated human body, Ind. Health 48 (2010) 682–697, https://doi.org/10.2486/indhealth.MSWBVI-25.
[34] G. Marini, G. Huber, K. Püschel, S.J. Ferguson, A 1-D model of the nonlinear dynamics of the human lumbar intervertebral disc, J. Sound Vib. 387 (2017) 194–206, https://doi.org/10.1016/j.jsv.2016.09.021.
[35] J.C. Iatridis, M. Weidenbaum, L.A. Setton, V.C. Mow, Is the nucleus pulposus a solid or a fluid? Mechanical behaviors of the nucleus pulposus of the human intervertebral disc, Spine 21 (1996) 1174–1184.

[36] H.J. Wilke, P. Neef, M. Caimi, T. Hoogland, L.E. Claes, New in vivo measurements of pressures in the intervertebral disc in daily life, Spine 24 (1999) 755–762.
[37] T.H. Smit, M.S. van Tunen, A.J. van der Veen, I. Kingma, J.H. van Dieën, Quantifying intervertebral disc mechanics: a new definition of the neutral zone, BMC Muscoskel. Disord. 12 (2011) 1–10, https://doi.org/10.1186/1471-2474-12-38.
[38] A. Shirazi-Adl, Analysis of large compression loads on lumbar spine in flexion and in torsion using a novel wrapping element, J. Biomech. 39 (2006) 267–275, https://doi.org/10.1016/j.jbiomech.2004.11.022.
[39] N. Arjmand, Computational Biomechanics of the Human Spine in Static Lifting Tasks, École Polytechnique de Montréal, 2006.
[40] N. An, Human Spine, grabCAD.com. https://grabcad.com/library/human-spine-1, 2014.
[41] D.C. Karnopp, D.L. Margolis, R.C. Rosenberg, 4, System Dynamics, Modeling and Simulation of Mechatronic Systems, 1990.
[42] N. Arjmand, A. Shirazi-Adl, B. Bazrgari, Wrapping of trunk thoracic extensor muscles influences muscle forces and spinal loads in lifting tasks, Clin. Biomech. 21 (2006) 668–675, https://doi.org/10.1016/j.clinbiomech.2006.03.006.
[43] L. Hansen, M. De Zee, J. Rasmussen, T.B. Andersen, C. Wong, E.B. Simonsen, Anatomy and biomechanics of the back muscles in the lumbar spine with reference to biomechanical modeling, Spine 31 (2006) 1888–1899, https://doi.org/10.1097/01.brs.0000229232.66090.58.
[44] C.E. Clauser, J.T. McConville, J.W. Young, Weight, Volume, and Center of Mass of Segments of the Human Body, Antioch Coll Yellow Springs OH, 1969.
[45] R. Chandler, C.E. Clauser, J.T. McConville, H. Reynolds, J.W. Young, Investigation of inertial properties of the human body, in: Air Force Aerospace Medical Research, Lab Wright-Patterson AFB OH, 1975.
[46] G. Papaioannou, A. Voutsinas, D. Koulocheris, I. Antoniadis, Dynamic performance analysis of vehicle seats with embedded negative stiffness elements, Veh. Syst. Dyn. (2019), https://doi.org/10.1080/00423114.2019.1617424.
[47] T.S. Keller, C.J. Colloca, J.-G. Béliveau, Force-deformation response of the lumbar spine: a sagittal plane model of posteroanterior manipulation and mobilization, Clin. Biomech. 17 (2002) 185–196, https://doi.org/10.1016/S0268-0033(02)00003-7.
[48] S.R. Ward, A. Tomiya, G.J. Regev, B.E. Thacker, R.C. Benzl, C.W. Kim, R.L. Lieber, Passive mechanical properties of the lumbar multifidus muscle support its role as a stabilizer, J. Biomech. 42 (2009) 1384–1389, https://doi.org/10.1016/j.jbiomech.2008.09.042.
[49] K.M. Moorhouse, K.P. Granata, Role of reflex dynamics in spinal stability: intrinsic muscle stiffness alone is insufficient for stability, J. Biomech. 40 (2007) 1058–1065, https://doi.org/10.1016/j.jbiomech.2006.04.018.
[50] R. Bayoglu, L. Geeraedts, K.H. Groenen, N. Verdonschot, B. Koopman, J. Homminga, Twente spine model: a complete and coherent dataset for musculo-skeletal modeling of the thoracic and cervical regions of the human spine, J. Biomech. 58 (2017) 52–63, https://doi.org/10.1016/j.jbiomech.2017.04.003.
[51] B. Bazrgari, A. Shirazi-Adl, M. Kasra, Computation of trunk muscle forces, spinal loads and stability in whole-body vibration, J. Sound Vib. 318 (2008) 1334–1347, https://doi.org/10.1016/j.jsv.2008.04.047.
[52] D. Karnopp, Vehicle Dynamics, Stability, and Control, CRC Press, 2013.
[53] M.Y. Svensson, O. Boström, J. Davidsson, H.-A. Hansson, Y. Håland, P. Lövsund, A. Suneson, A. Säljö, Neck injuries in car collisions—a review covering a possible injury mechanism and the development of a new rear-impact dummy, Accid. Anal. Prev. 32 (2000) 167–175, https://doi.org/10.1016/S0001-4575(99)00080-9.
[54] P. Russell, M. Pearcy, A. Unsworth, Measurement of the range and coupled movements observed in the lumbar spine, Rheumatology 32 (1993) 490–497, https://doi.org/10.1093/rheumatology/32.6.490.